

Robust coherent dynamics of homogeneously limited anisotropic excitons in two-dimensional layered ReS₂

*Rup Kumar Chowdhury**, *Md Samiul Islam*, *Marie Barthelemy*, *Nicolas Beyer*, *Lorry Engel*,

Jean-Sébastien Pelle, *Mircea Rastei*, *Alberto Barsella*, and *Francois Fras* *

Université de Strasbourg, CNRS, Institut de Physique et Chimie des Matériaux de

Strasbourg, UMR 7504, F-67000 Strasbourg, France

Abstract

The discovery of in-plane anisotropic excitons in two-dimensional layered semiconductors enables state-of-the-art nanophotonic applications. A fundamental yet unknown parameter of these quasiparticles is the coherence time (T_2), which governs the quantum dephasing timescale, over which the coherent superposition of excitons can be maintained and manipulated. Here, we report the direct measurement of T_2 within the sub-picosecond range, along with multiple population decay timescales (T_1) at resonance for anisotropic excitons in pristine layered rhenium disulfide (ReS₂). We observe a notable weak dependence on layer thickness for T_2 , and a quasi-independence for T_1 . The excitonic coherence in few-layer ReS₂ exhibits exceptional robustness against optical density and temperature compared to other two-dimensional semiconductors, enabling quantum features even at room temperature. No photon echo fingerprints were observed in pristine ReS₂, highlighting the homogeneous character of the anisotropic excitonic transitions and a particularly low level of disorder in exfoliated flakes. Lastly, our results for mono- to bulk-like ReS₂ support a direct gap band structure regardless their layer thickness, addressing the ongoing discussion about its nature.

Introduction

Transition metal dichalcogenides (TMDCs) are van der Waals (vdW) materials that can be processed to an atomically thin level, with impressive structural and optical properties, including chemical stability, mechanical flexibility, and high oscillator strength [1-2]. Their exceptional exciton binding energies enable stable Coulomb-bound excitons even at room temperature [3]. Additionally, their two-dimensional (2D) nature allows easy integration into photonic chips [4-5] and heterostructure devices [6-7].

Alternatively, vdW materials with intrinsic anisotropic characteristics have attracted a particular research interest. Unlike highly symmetric hexagonal (2H) group-VI TMDCs namely MX_2 ($\text{M} = \text{Mo}, \text{W}$; and $\text{X} = \text{S}, \text{Se}$) [1-3], two members of group-VII TMDCs (ReX_2) display strong in-plane anisotropic structure with distorted octahedral phase (1T') and reduced lattice symmetry [8]. Owing to the Jahn-Teller like structural distortion and a zigzag Re-Re chainlike structure (b-axis), a pair of anisotropic excitons emerges naturally inside ReX_2 lattices on their 2D planes (Fig. 1a) [9-10], which then exhibits certain one-dimensional excitonic aspects [11-12] even without strain engineering [13]. ReX_2 exhibits fundamental phenomena like exciton-polaritons and quantum beating [14-15], while remaining stable under ambient conditions, unlike anisotropic black phosphorus [16-17], making it suitable for polarization-sensitive optoelectronics [18-19].

Unlike traditional MX_2 showing direct band exciton transition only in its monolayer limit [1-2], the excitonic optical response of ReX_2 persists when increasing the layer numbers due to weak interlayer coupling [9]. The band structure appears to be independent of the layer numbers, leading to a monolayer-like electronic structure in bulk ReX_2 . Yet, the fundamental question of whether the gap is truly direct or indirect is the subject of active debate to date [20-21]. In this context, time-resolved experiments can provide valuable insights. Earlier reports with time-resolved non-resonant approaches indicate exciton population dynamics within 10-100 ps [22-26], although they cannot infer sub-picosecond dynamics due to either limited time resolution or the involvement of charge relaxation pathways leading to exciton formation, potentially hindering the exploration of intrinsic dynamics at the excitonic levels. Moreover, excitonic linewidths in bare MX_2 are mainly dominated by inhomogeneous contributions [27-29], and even after hexagonal boron nitride (hBN) encapsulation, local disorder still persists [30-32]. Regarding anisotropic 2D semiconductors like ReX_2 , both the role of disorder in the excitonic linewidth and the coherence properties, characterized by the coherence time T_2 (related to the homogeneous linewidth γ by $T_2 = 2\hbar/\gamma$), remain as open questions.

Resonant four-wave mixing (FWM) spectroscopy is particularly suitable for addressing these questions [28-29, 33-34], providing a direct pathway to investigate the dynamics of exciton coherence and population by resonantly exciting specific optical transitions. However, the exciton properties varies with the orientation (b-axis) and thickness of each ReX_2 flakes [9, 35-36]. Therefore, a microscopic approach is essential. In this context, combining FWM time-resolved spectroscopy with microscopy presents a notable challenge.

Here, we performed state-of-the-art FWM micro-spectroscopy based on optical heterodyning and spectral interferences [37]. This experimental configuration allows to probe areas with

spatial resolution limited by diffraction and a temporal resolution determined by pulse duration (~ 100 fs). We investigated the coherence and population dynamics of spectrally selective anisotropic excitons while varying key parameters such as: (i) temperature, (ii) optical power, (iii) flake locations and thickness. We found that T_2 is in the hundreds of femtoseconds and remains particularly robust against increases in optical power and temperature, continuing to exhibit measurable coherent signatures even at room temperature. We observed that the corresponding excitonic linewidth is homogeneously limited, suggesting low disorder level in bare ReS₂. These unique characteristics distinguish them from other layered MX₂ semiconductors [31-32]. The exciton population dynamics reveal multiple exponential components, ranging from ~ 150 fs to the nanosecond scale, involving scattering between bright and dark excitonic states. These intrinsic dynamics are consistent with a direct bandgap, regardless of the number of ReS₂ layers.

Results

ReS₂ sample was prepared *via* mechanical exfoliation (see Methods). Six different flakes were investigated, identified in white light imaging by their contrast (Fig. 1b), and in atomic force microscopy by their thickness ranging from bulk-like (Flake-1) to monolayer (Flake-6) (Fig. 1c and Fig. S1, supplementary information (SI)). The optical emission from layered ReS₂ is dominated by excitonic transitions [9-10, 38]. The exciton resonances are first identified from the hyperspectral PL imaging (Fig. 1d) of which a spectrum example is presented in Fig. 1e, featuring two peaks associated with the anisotropic excitons EX₁₍₂₎ at ~ 1.54 (1.57) eV.

Following the PL characterizations of EX_{1,2}, we performed FWM micro-spectroscopy (details in Methods, SI-Sec. 2, and [37]) to investigate their coherent dynamics (Fig. 2). FWM arises from third-order nonlinearity involving three interactions between the optical pulses and the system. The first interaction induces a coherent polarization in the sample, which is converted into a population by the second interaction, and the third one interacts with the latter population to yield the FWM signals. We employed two configurations. In the first (Fig. 2a), we utilized two pulses ($E_{1,2}$), leading to a FWM field $\propto \mu^4 E_1^* E_2^2$, with μ the electric dipole moment. $E_{1,2}$ are temporally separated by a delay (τ_{12}), allowing to retrieve the dynamics of excitonic coherences. In the second configuration (Fig. 2b), three pulses ($E_{1,2,3}$) were employed with E_1 and E_2 overlapping ($\tau_{12} \approx 0$). The FWM signal $\propto \mu^4 E_1^* E_2 E_3$ is monitored as a function of the delay (τ_{23}) between E_2 and E_3 , enabling to retrieve the dynamics of excitonic population. The heterodyne detection technique allows FWM to be conducted with collinear pulse beams by

radiofrequency ($\Omega_{1,2,3}$) shifting the pulse trains. The FWM field is subsequently detected via spectral interference with a reference beam, as exemplified in Fig. 2d.

Coherence dynamics. To optimize the FWM signal for each exciton $EX_{1,2}$, we first analyzed the linear polarization-resolved FWM signal in the two-pulse configuration with a fixed τ_{12} , and determined the local dipole orientations under resonant conditions for excitons $EX_{1,2}$ (Fig. 2e). The signal exhibits a $\cos^4(\theta - \theta_0)$ behaviour, where θ is the excitation polarization angle. This results from three interactions with electric fields, leading to FWM signal, and the fourth power from its projection onto the reference beam. We observe a twist of about 70° in the two linear dipoles, consistent with prior findings [10, 39].

We now consider the excitonic coherent dynamics as a function of τ_{12} . In this configuration, FWM spectroscopy offers the fundamental advantage of deciphering coherence loss through homogeneous broadening γ and coherence dephasing due to inhomogeneous broadening σ . We begin by evaluating the relative weight of σ to γ at 10 K, where it is expected to be the highest. To achieve this, the method is as follows: we initially examine the FWM dynamics in the 2D variables framework (τ_{12} , t), obtained by Fourier transformation (see Methods), where a significant inhomogeneous contribution σ should exhibit a clear photon echo signature. Figure 2f-g presents a 2D FWM plot at 10 K for both $EX_{1,2}$, for the multilayer Flake-2 (additional data for monolayer Flake-6 in Fig. S3, SI). Remarkably, we do not observe photon echo formation for both $EX_{1,2}$ as the maximum amplitude of the FWM signal does not follow the diagonal $t = \tau_{12}$. Instead, the signal evolves as free induction decay, suggesting a weak inhomogeneous contribution satisfying the condition $\sigma \ll \gamma$. Based on this initial estimation, the next step involves evaluating γ and the upper bound of σ by fitting the FWM amplitude as a function of τ_{12} (Fig. 2h-i). The fitting function accounts for the convolution of the pulse shape with the system response, characterized by an exponential decay of coherence (γ) and Gaussian-like inhomogeneous dephasing (σ). Further details of the fitting function are provided in SI-Sec. 3. For thick multilayer and monolayer ReS_2 , γ is around 5 meV and 8 meV respectively (Fig. 2h-i and Fig. S3, SI), while σ remains negligible independently of flake thickness, with an upper bound of $\sigma \leq 1.0$ meV, as determined by the consistent fit quality up to this limit. The weak dependence of γ on flake thickness at 10 K is shown in more detail in Fig. 3h. Complementary data at 77 K exhibits a similar trend (Fig. S5). We conclude that, even when thinning down to the monolayer limit, the exciton coherent dynamics in pristine ReS_2 are governed by the homogeneous contribution γ . In contrast, conventional MX_2 shows such behavior only when

encapsulated in hBN [32-33]. Comparatively, in bare monolayer MoSe₂, exciton dynamics show a clear photon echo with a large σ ranging between 7 to 15 meV [29].

We now present the detailed evolution of γ or coherence time ($T_2 = 2\hbar/\gamma$) as a function of (i) temperature, (ii) optical power, and (iii) flake locations, as summarized in Fig. 3 and Fig. S4. First we explore the robustness of the excitonic coherences against sample temperature (T) and the resulting exciton-phonon interaction. Examples of FWM dynamics on multilayer Flake-2 with respect to temperature variations are shown in Fig. 3a-b, while $\gamma(T)$ for EX₁₋₂ is presented in Fig. 3c-d. Interestingly, $\gamma(T)$ exhibits notable linear variations even up to room temperature, allowing extraction of the homogeneous limit γ_0 at zero temperature, approximately 3.9 ± 0.8 (5.8 ± 0.9) meV for EX₂₍₁₎. Importantly, the coherent signature dynamics remain discernible, although approaching our time resolution limit, even at room temperature. This contrasts with MX₂ systems, where γ becomes unresolved above ~ 120 K [29-32] (under similar experimental temporal resolution), highlighting ReS₂ specific robustness against temperature-induced decoherence. This pronounced linear behavior also differs from the well-reported parabolic trend of $\gamma(T)$ in MX₂ [29-32]. The thermal broadening of γ is analyzed in more detail using the expression $\gamma(T) = \gamma_0 + \alpha T + \beta \left(\exp\left(\frac{E_0}{k_B T}\right) - 1 \right)^{-1}$, where 2nd and 3rd components represent the contributions of low-energy acoustic phonons and high-energy optical phonons, respectively. This arises from the phonon occupation number, with the linear dependence on T for acoustic phonons due to the assumption that the energies of interacting acoustic phonons, constrained by momentum conservation, are less than the thermal energy $k_B T$. For both EX_{1,2}, the acoustic-phonon scattering value α is extracted around 33 ± 15 $\mu\text{eV/K}$. However, using this approach for the optical part, several pairs of E_0 and β fit our data, with E_0 varying from 50 to 200 meV and β from a few meV to 2.0 eV. Therefore, based on a recent estimation of E_0 [39], we constrained E_0 to around 50 meV and, from fitting, found it to be 61 (44) meV, with β being 5.0 ± 2.6 (6.3 ± 1.1) meV for EX₁₍₂₎, respectively. Finally, the extracted value of optical phonon coupling β in ReS₂ is approximately 30 times lower than in MoSe₂ and WSe₂ monolayers [29, 31] for similar activation energy and acoustic phonon coupling, quantifying the particular robustness of ReS₂ excitonic coherence with temperature. Such pronounced linear behavior of $\gamma(T)$, associated with relatively weak optical phonon coupling, is unexpectedly similar to the findings in single carbon nanotube systems [40-41]. One approach to further elucidate this behavior in 2D ReS₂ could involve the one-dimensional aspect of Re-chains due to strong structural anisotropy [11, 42].

Another important parameter that can influence γ is the exciton density that can be directly controlled by the pump (E_1) power density P . With increasing P , exciton-exciton interaction leads to excitation induced dephasing (EID) [29, 33]. Power dependent FWM experiments have consistently reported a linear trend in $\gamma(P)$ within the range of 10^2 - 10^3 W/cm² for bare and hBN encapsulated MX₂ monolayers [29, 33]. In ReS₂, we measure $\gamma(P)$ up to 2.5×10^5 W/cm² exhibiting two distinct quasi-linear characteristics (Fig. 3e-f). We then analysed the behaviour, in each region, using: $\gamma(P) = \gamma_{P0} + A \times P$, where γ_{P0} is the zero-power linewidth and A is a coefficient related to exciton-exciton interaction. Individual fits and extracted parameters are presented in Fig. S6 (SI). Under low power conditions (Region-I), A is extracted around 5×10^{-4} meVcm²/W at 10 K, which is an order of magnitude smaller compared to MX₂ [33] (with similar pulse length and repetition rate), indicating reduced EID. Complementary data obtained at 77 K shows similar behaviours (Fig. S6), emphasizing robust coherence characteristics of EX_{1,2} against optical density. We conclude the study of exciton coherence by exploring the influence of flake spatial location. Figure 3g shows γ for both EX_{1,2} across multiple locations on Flake-2 (spanning ~ 10 μ m), with weak spatial dispersion, indicating uniform excitonic behavior. This complements the low microscopic disorder (negligible σ) probed under diffraction-limited beams as discussed above.

Population dynamics. We next employ three-pulse ($E_{1,2,3}$) resonant excitation scheme (Fig. 2b) to probe the EX_{1,2} population dynamics. At $\tau_{12} \approx 0$, the polarization selective resonant pumping creates an initial density of excitons within the light cone (Fig. 4a). These excitons subsequently relax through radiative and non-radiative channels. To analyse the interplay among these channels, we also recorded population dynamics as a function of power, temperature, and flake thickness (Fig S8-10). Figure 4b shows examples of population dynamics of EX₁ in with varying density and temperature. The dynamics suggest that population decays (T_1) EX_{1,2} across multiple timescales, spanning from hundreds of femtoseconds to nanoseconds. Unlike in MX₂ [31, 43], we did not observe any variation in the FWM phase with τ_{23} , which would lead to population modulations. Thus, population dynamics are well-fitted using a multi-exponential transient response function, $R(\tau_{23}) \propto \sum_{n=1}^3 A_n \theta(\tau_{23}) \exp\left(-\frac{\tau_{23}}{T_{1n}}\right)$, convoluted with a Gaussian pulse (SI Sec. 5), where $\theta(\tau_{23})$ represents the Heaviside function. This approach allows us to extract three distinct lifetime components (T_{1n}) and relative amplitudes A_n/A for both EX_{1,2} (Fig. 4c-d) under different experimental conditions (complementary data in SI, Sec. 6-7). To avoid ambiguities in the short-time-scale analysis, we conducted alternative curve fits (details in SI-Sec. 5) using i) only

two measurable decay times, and ii) three decay channels, with the first considered instantaneous relative to the resolution ($T_{11} \ll$ pulse-duration), for instance due to a non-resonant contribution [23-24]. These fits resulted in lower quality, demonstrating the relevance of the three-resolvable-decay-channel analysis. For both excitons, we found an extremely fast initial decay channel T_{11} with a characteristic time of approximately 150 fs, varying slightly with temperature, power, and flake thickness parameters. Following this, the second exponential component T_{12} ranges from 0.5 to 1.0 ps and shows a similar relative amplitude to the initial component ($A_1/A \approx A_2/A$). The third decay timescale (T_{13}) exceeds nanosecond window for both excitons, with relative amplitude of $A_3/A \approx 2A_1/A$ at low power and temperature. Such ultrafast dynamics, featuring a 150 fs component, are consistent with previous findings on MX_2 systems performed at resonance [30-31, 44-45], however it contrasts with non-resonant studies on ReS_2 , which only highlighted dynamics in the range of 10-100 ps [23-24].

Importantly, the population dynamics (T_{1n} and A_n/A) remain largely independent of flake thickness (see SI-Sec. 6-7), consistent with an unchanged band structure across varying numbers of layer [9]. To explore the mechanisms controlling population dynamics, we analyzed all three T_1 components as a function of optical power and temperature (Fig. 4b-d). With increasing optical power and temperature, all time components decrease. Additionally, the weight of the third channel decreases, while the proportion of the second channel (A_2/A) increases, becoming dominant at room temperature. Such multiscale dynamics suggest a strong connection between bright and dark state reservoirs [20, 29, 39, 43-44] comprising excitons with in-plane momentum outside the light cone, and spin-forbidden dark states lying tens of meV below the bright states as recently revealed [20]. Indeed, exciton scattering is highly efficient in TMDCs, particularly due to their relatively large exciton mass, wide exciton linewidth, and small conduction band splitting [1-2]. Therefore, bright excitons can significantly scatter into dark state reservoirs through non-radiative processes, such as exciton-phonon and exciton-exciton scatterings, including the Auger process, which exhibits high efficiency in WSe_2 monolayer [44]. With temperature and excitation density, these processes enhance their efficiency, effectively dominating the population dynamics. The different decay times of the dynamics result from a combination of the scattering processes between excited states and irreversible decay processes into the ground state. In this framework, the shortest component (T_{11}) arises from both radiative decay and exciton scattering from bright to dark states. The second (T_{12}) and third components (T_{13}) result from the population decay of the dark reservoirs, including the return of the exciton into the light cone via secondary scattering.

Additionally, the population dynamics of EX₁ and EX₂ are notably similar across different temperatures and excitation densities (see Fig. 4c-d and SI-Sec. 6-7). This similarity, especially at low temperatures despite the 30 meV excitons splitting, suggests that inter-valley EX₁-EX₂ scattering plays a negligible role in population dynamics compared to other scattering mechanisms discussed.

Conclusion

Our analysis reveals that T_1 and T_2 values for layered ReS₂ are comparable to what is observed in MX₂ monolayers [27-32, 43-44], which exhibit direct band gap characteristics. On contrary, indirect gap bilayer MoSe₂ [46] exhibits ultrashort T_1 (60 and 800 fs) and T_2 (50 fs) values at 30 K that are an order of magnitude smaller than the monolayer due to the complex indirect band structure of MX₂ bilayers, allowing multiple ultrafast excitonic scattering pathways. Additionally, the enhancement of exciton-photon scattering times due to the indirect band gap was estimated to be around 10 fs in WS₂ bilayers [47]. Therefore, our findings on ReS₂ suggest an electronic structure featuring a direct band gap regardless of layer thickness, which was suggested earlier using angle-resolved (k -space) photoemission spectroscopies on bulk [42] and atomically thin ReS₂ [48]. In summary, we investigated the intrinsic T_2 and T_1 characteristic times of excitons in anisotropic ReS₂ layered systems using ultrafast four-wave mixing microscopy under resonant conditions. We found that the excitonic linewidth γ is homogeneously dominated, while the population dynamics T_1 involved ultrafast non-radiative processes. We observed that T_2 shows a weak dependence on layer thickness, while T_1 remains almost independent of it. Compared to the excitonic coherence in MX₂ TMDCs, few-layer ReS₂ displays impressive robustness against optical density and temperature, enabling room-temperature quantum features. The large scale spatial homogeneity of T_2 and the negligible inhomogeneous contribution indicate a particularly low level of excitonic disorder in exfoliated flakes. Our findings thus provide fundamental insights into low-dimensional anisotropic layered ReS₂, highlighting that it offers the advantages of MX₂ monolayer-like direct band excitonic properties combined with the robustness provided by the multilayer form.

METHODS

Sample fabrication and characterization. A commercially available quasi-transparent flat sapphire was used as the substrate, which was cleaned using Ar plasma (2 min) before proceeding with ReS₂ sample preparation. The ReS₂ flakes were mechanically exfoliated from a crystal (2D semiconductor) using standard scotch-tape and directly transferred on the sapphire after thinning down. Following this, the identification of the flakes and characterization of their thicknesses were performed using a white light optical microscope and an atomic force microscope.

PL and FWM micro-spectroscopy set-up. We developed a dual-mode experimental setup for PL and FWM spectroscopy, with confocal spatial mapping, using a 0.9 NA objective to focus the excitation spot to the diffraction limit. For PL measurements, we used a continuous-wave 532 nm laser to non-resonantly excite our layered ReS₂ sample. The excitonic emission was collected via a spectrometer (monochromator + CCD camera) with a spectral resolution of ~ 0.02 nm. The sample was placed inside a cryostat equipped with position-controlled piezoelectric nanopositioner stages. The optical pulses for FWM measurements were generated with a spectrally tunable Ti: sapphire laser oscillator with 80 MHz repetition rate. All pulses were then passed through a single-prism pulse compressor to minimize the pulse duration at the sample location. The full width at half maximum (FWHM) of the Gaussian pulses was determined to be $115 \text{ fs} \pm 10 \text{ fs}$ from autocorrelator measurements and fixed at 118 fs in the FWM modeling (see SI Sec. 3). The temporal acquisition is achieved using a mechanical delay line that provides time-delayed collinear optical pulses. Linear polarizations, along with the spectral resolution, were used to address EX₁ and EX₂ individually. We separately measured the transient excitonic coherence and population signals using two-pulse (E_{1,2}) and three-pulse (E_{1,2,3}) sequence configurations, respectively. The FWM is detected using optical heterodyne and spectral interferometry [37, 49]. The time-delayed excitation pulses, E_{1,2} and E_{1,2,3}, were frequency upshifted by distinct radio-frequencies (RF) Ω_i around 110 MHz using acousto-optic modulators (AOM) drive by a custom-built RF mixer. The relatively weak FWM signal appearing at the FWM frequencies $2\Omega_2 - \Omega_1$ (E_{1,2}) or $\Omega_3 + \Omega_2 - \Omega_1$ (E_{1,2,3}), also around 110 MHz, differed from the excitation pulses radio frequencies Ω_i . Then the signal was retrieved through spectral interference with a reference pulse, and detected using the spectrometer. The spectrally detected FWM signals, dependent on the pulse delay τ_{12} (coherence dynamics) or τ_{23} (population dynamics), were processed using fast Fourier transformations (FFT). This led to the extraction of both FWM phase and amplitude in either the time domain (single FFT) or

frequency domain (FFT followed by a reverse FFT) [45, 49]. Therefore, the FWM amplitude is analyzed in the 2D frame (t, τ) or (ω, τ) , or integrated over the frequency resonance of each exciton and presented as a function of τ , referred to in the main text as FWM dynamics.

FIGURES

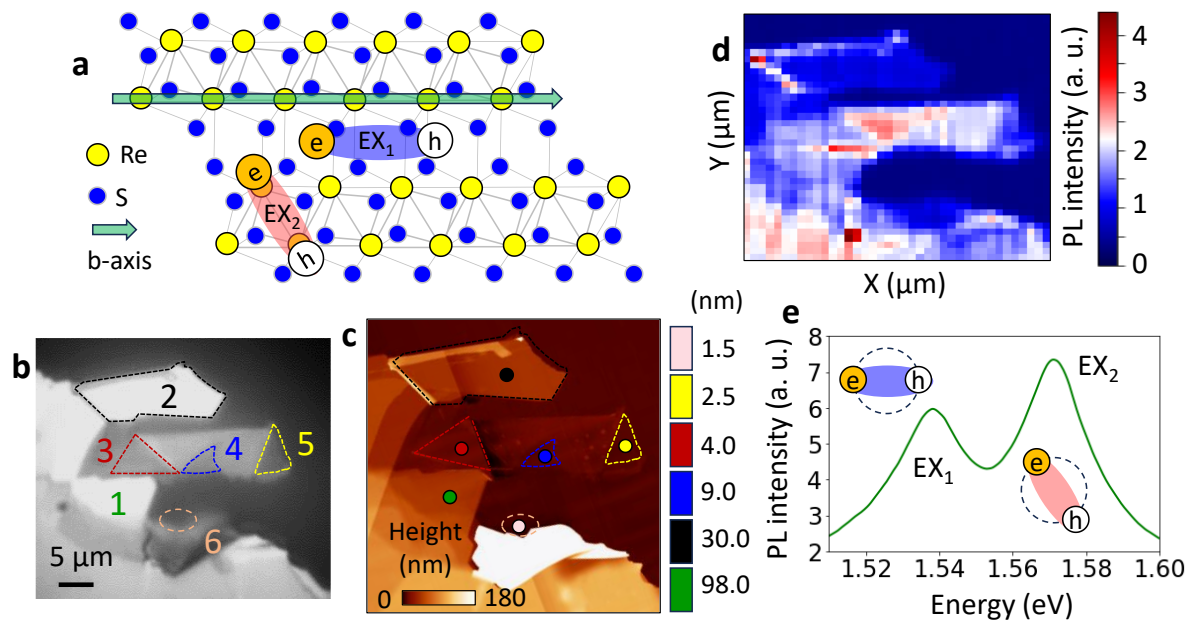


Fig. 1 | Basic morphological and optical characterizations of layered ReS₂. **a**, Schematic top view of a ReS₂ layer with in-plane anisotropic exciton pair (EX₁ and EX₂). Green arrow denotes the crystalline b-axis (along Re-Re chains). Yellow and blue dots characterize Re and S atoms, respectively. **b**, White light image of mechanically exfoliated ReS₂ flakes with different thickness. The different flakes studied are marked by the dashed lines and indicated by their flake numbers starting from Flake-1 to Flake-6. The scale bar is 5.0 μm. **c**, Atomic force micrograph of the ReS₂ flake locations with corresponding colour bar in the insets denoting height profiles of flakes marked with individual colours (vertical) and overall height profiles (horizontal). The thickness data extracted from AFM measurement for Flake-1 to 6 appeared as bulk-like (green), multilayers (black), few-layers (blue), 3-4 layered (brown), 2-3 layered (yellow), and 1-2 layered (pink) flakes, respectively. **d**, Hyperspectral PL map (77 K) (integrated over the entire spectral window range) of the flakes with the associated PL intensity colour scale. The step size is 1.0 μm. **e**, Typical PL spectrum taken on Flake-2, highlighting the two lowest energy optically bright excitons (EX₁ and EX₂) with schematic representation as shown in the inset.

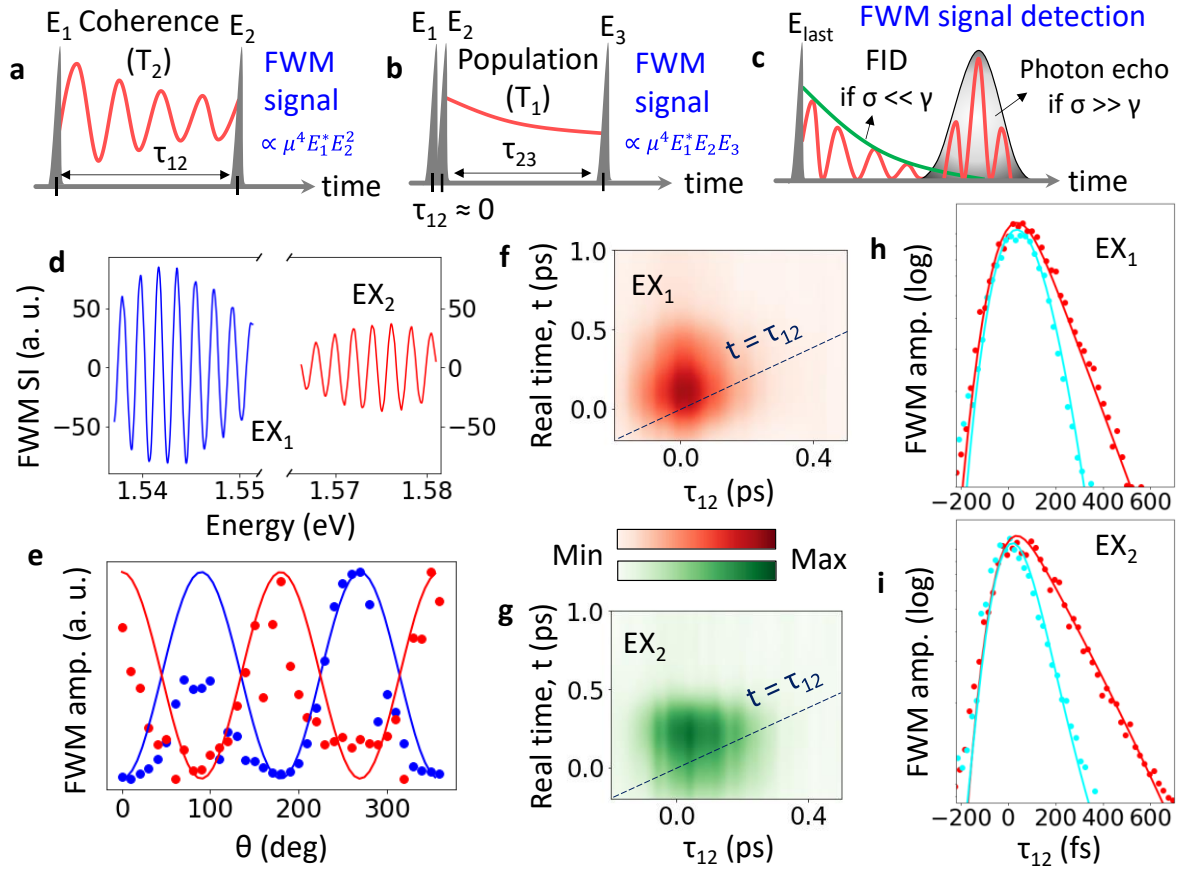


Fig. 2 | Resonant FWM micro-spectroscopy on layered ReS₂. **a**, Schematic representation of two pulse (E_1 and E_2) configurations, varying τ_{12} allow to probe the dynamics of coherences, characterised by coherence time T_2 . **b**, Three pulse (E_1 , E_2 , and E_3) configurations, with E_1 and E_2 overlapping ($\tau_{12} \approx 0$), varying τ_{23} allows to probe the dynamics of exciton population. The description of the pulse sequence on the system is provided in the main text and method part. **c**, Representation in real time, t of FWM for two situations: when homogenous contribution dominates called free induction decay (FID) and when inhomogeneous contribution dominates called photon echo, where the maximum of the echo is at $t = \tau_{12}$. E_{last} in the schematic diagram represents E_2 in two pulse and E_3 in three pulse configurations. **d**, Example of FWM signal: spectral interferograms of EX₁ (blue line) and EX₂ (red line) obtained at resonant excitonic energies recorded for a specific delay value τ_{12} . From these interferograms, the FWM amplitude, either in time or spectrum, is extracted through Fourier analysis (see Methods and SI) for each delay τ_{12} . **e**, FWM amplitude, at $\tau_{12} \approx 0$, as a function of $E_{1,2}$ linear polarization angle (identical for both beams) for both EX₁ (blue dots) and EX₂ (red dots) with the corresponding fits (solid lines). FWM amplitudes resolved in function of real time t and delays τ_{12} for **f**, EX₁ and **g**, EX₂ with corresponding colour scale for multilayer Flake-2. Examples of

FWM amplitudes versus τ_{12} presented for **h**, EX₁ and **i**, EX₂ at 10 K and 50 W/cm² along with the corresponding fits (solid lines) for monolayer (cyan) and multilayer (red) ReS₂ flake.

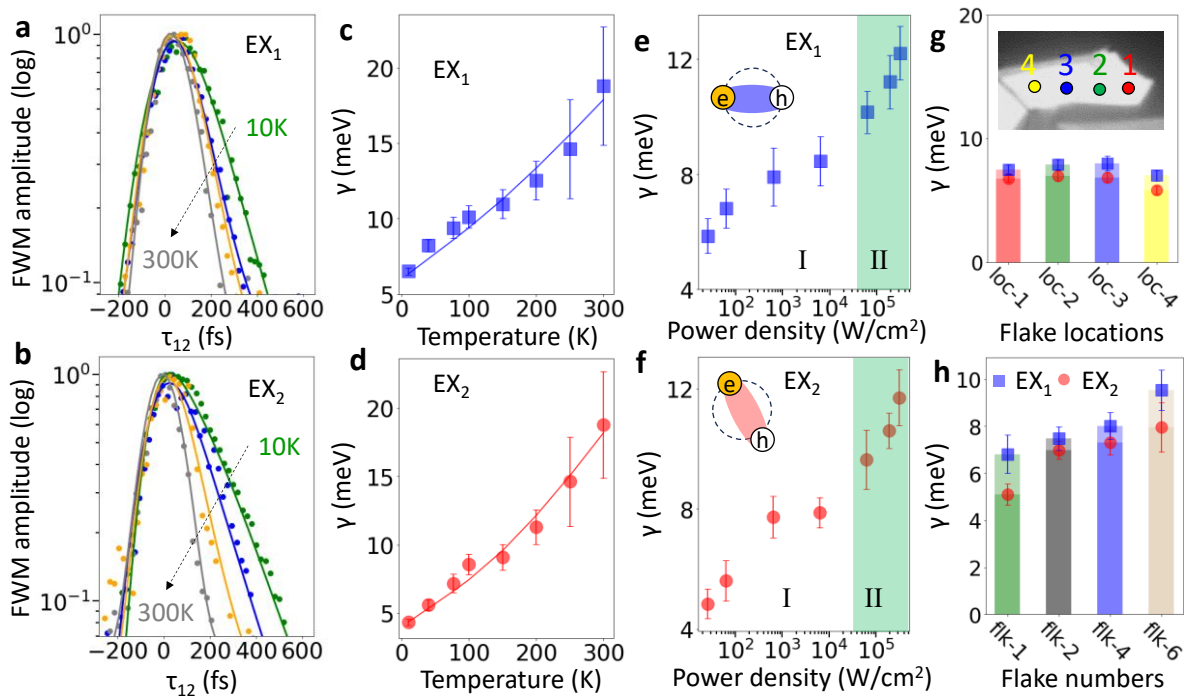


Fig. 3 | Coherent dynamics of anisotropic excitons in layered ReS₂. Examples of FWM amplitudes versus τ_{12} presented for **a**, EX₁ and **b**, EX₂ at several temperatures starting from 10 K to 300 K, along with the corresponding fits (solid lines) on Flake-2. Variation of γ , with corresponding fits, for **c**, **e**, EX₁ and **d**, **f**, EX₂ in function of temperatures and power density, respectively. Temperature dependent measurements shown in figure (c) and (d) performed at fixed pump power density 50 W/cm². Solid lines denote fits, with extracted parameters of temperature induced dephasing, are discussed in the main text. Conversely, power dependent measurements shown in figure (e) and (f) were conducted at a fixed temperature of 10 K. Two regions are marked based on power density: I with power density < 10⁴ W/cm² (white shaded area) and II with power density > 10⁴ W/cm² (green shaded area). Both regions exhibit distinct linear behaviours with different slopes. Inset of (e) and (f): schematic images of in-plane anisotropic excitons in ReS₂ with different dipolar orientations. **g**, Distribution of γ for different locations on Flake-2. The inset shows different measurement locations on Flake-2, corresponding to colour codes of the bars. **h**, Homogeneous linewidth (γ) for EX₁ (blue) and EX₂ (red) as a function of flake numbers, where flake thickness decreases with increasing flake numbers as discussed in AFM analysis. Measurements in (g) and (h) were conducted at 10 K and 50 W/cm².

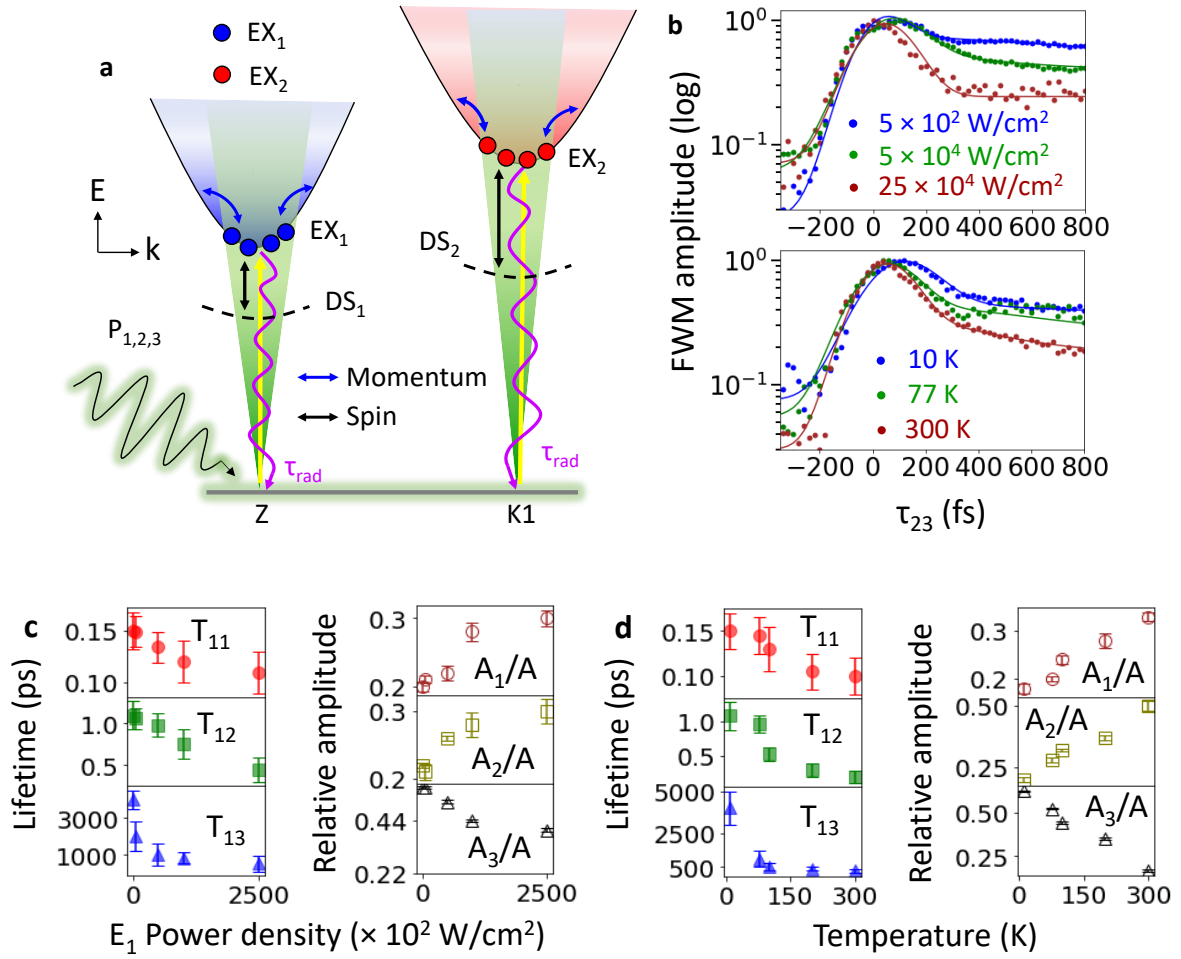


Fig. 4 | Population dynamics of anisotropic excitons in layered ReS₂. **a**, Schematic of the energy level dispersion (E, k), including optical transition and scattering processes, within the hypothetical framework of the two valleys (Z and K1) in ReS₂. The spin-allowed excitonic transition bands comprising the excitonic bright states EX_{1,2} (blue and red solid circles), which lie within the light cones (green shaded areas) and are split by 30 meV (see Fig. 1e). DS_{1,2} designates the spin-dark states (no direct optical transition allowed), which, according to Ref. [20], are located 13 meV (20 meV) below EX₁₍₂₎. The resonant optical excitations of EX_{1,2} are depicted as yellow solid lines. From the light cone, EX_{1,2} excitons can radiatively recombine (purple curved arrow), scatter to momentum-dark states outside the light cone (blue solid line), or scatter to spin-dark states DS_{1,2} (black solid line). **b**, Examples of pump (E_1) power density and temperatures dependent population dynamics of EX₁ in terms of FWM field amplitude data with corresponding fits (solid lines) as function of the $E_{2,3}$ delay τ_{23} . The power (temperature) dependent measurements are carried out at fixed temperature (power density): 10 K (50 W/cm²). **c, d**, Summary of each transient FWM population dynamics fitting lifetimes (solid markers) and relative amplitudes (open markers) and corresponding errors represented

as error bars based on different parameters: power density and temperature for EX₁. Three different population timescales: T_{11} (red), T_{12} (green), and T_{13} (blue) along with corresponding relative amplitudes A_1/A (brown), A_2/A (olive), and A_3/A (black) of the decay processes are mentioned with different coloured markers. Here $A = A_1 + A_2 + A_3$. Note that the longest decay component (\sim ns range) is accurately determined from the experiments conducted over an extended delay range, as shown in Fig. SI-S11. The data here were recorded on multilayer Flake-2.

AUTHORS CONTRIBUTIONS

The project was originally proposed by FF. FF and MI built the experimental setup, with help from RC and MB. RC and MI carried out measurements, with help from MB and FF. RC and FF analysed the data with inputs from MI MB and AB. FF, RC, and MI conceived the analysis tools. RC fabricated the samples. NB, JP and LE provided a technical support. MR carried out the AFM measurements. FF and RC wrote the manuscript, with inputs from of MB MR and AB. FF supervised the project.

*Corresponding authors: fras@ipcms.unistra.fr, chowdhury@ipcms.unistra.fr

FUNDING SOURCES

This research was supported by the French Agence Nationale de Recherche (ANR) under the grants FINDING ANR-18-CE30-0012-01 and LHNANOMAT ANR-19-CE09-0006, and from the QUSTEC program (European Union's Horizon 2020, Marie Skłodowska-Curie Grant Agreement No. 847471).

REFERENCES

1. Mak, K. F., He, K., Lee, C., Lee, G. H., Hone, J., Heinz, T. F. & Shan, J. Tightly Bound Trions in Monolayer MoS₂. *Nat. Mater.* **12**, 207–211 (2013).
2. Chernikov, A., Berkelbach, T. C., Hill, H. M., Rigosi, A., Li, Y., Aslan, B., Reichman, D. R., Hybertsen, M. S. & Heinz, T. F. Exciton Binding Energy and Nonhydrogenic Rydberg Series in Monolayer WS₂. *Phys. Rev. Lett.* **113**, 076802 (2014).
3. Ross, J. S., Wu, S., Yu, H., Ghimire, N. J., Jones, A. M., Aivazian, G., Yan, J., Mandrus, D. G., Xiao, D., Yao, W. & Xu, X. Electrical Control of Neutral and Charged Excitons in a Monolayer Semiconductor. *Nat. Commun.* **4**, 1474 (2013).
4. Mak, K. F. & Shan, J. Photonics and Optoelectronics of 2D Semiconductor Transition Metal Dichalcogenides. *Nat. Photonics* **10**, 216–226 (2016).
5. Datta, I., Chae, S. H., Bhatt, G. R., Tadayon, M. A., Li, B., Yu, Y., Park, C., Park, J., Cao, L., Basov, D. N., Hone, J. & Lipson, M. Low-Loss Composite Photonic Platform Based on 2D Semiconductor Monolayers. *Nat. Photonics* **14**, 256–262 (2020).
6. Guo, H., Hu, Z., Liu, Z. & Tian, J. Stacking of 2D Materials. *Adv. Funct. Mater.* **31**, 2007810 (2021).
7. Qian, C., Troue, M., Figueiredo, J., Soubelet, P., Villafaña, V., Beierlein, J., Klemmt, S., Stier, A.V., Höfling, S., Holleitner, A.W. & Finley, J. J. Lasing of moiré trapped MoSe₂/WSe₂ interlayer excitons coupled to a nanocavity. *Sci. Adv.* **10**, eadk6359 (2024).
8. Satheesh, P. P., Jang, H.S., Pandit, B., Chandramohan, S. & Heo, K. 2D Rhenium Dichalcogenides: From Fundamental Properties to Recent Advances in Photodetector Technology. *Adv. Funct. Mater.* **33**, 2212167 (2023).
9. Tongay, S., Sahin, H., Ko, C., Luce, A., Fan, W., Liu, K., Zhou, J., Huang, Y. S., Ho, C. H., Yan, J., Ogletree, D. F., Aloni S., Ji J., Li S., Li J., Peeters F. M. & Wu J. Monolayer behaviour in bulk ReS₂ due to electronic and vibrational decoupling. *Nat. Commun.* **5**, 1-6 (2014).
10. Aslan, B., Chenet, D. A., Van Der Zande, A. M., Hone, J. C. & Heinz, T. F. Linearly polarized excitons in single-and few-layer ReS₂ crystals. *ACS Photonics* **3**, 96-101 (2015).
11. Kim, B. S., Kyung, W. S., Denlinger, J. D., Kim, C. & Park, S. R. Strong one-dimensional characteristics of hole-carriers in ReS₂ and ReSe₂. *Sci. Rep.* **9**, 2730 (2019).
12. Usman, A., Aly, M. A., Masenda, H., Thompson, J. J., Gunasekera, S. M., Mucha-Kruczyński, M., Brem, S., Malic, E. & Koch, M. Enhanced excitonic features in an anisotropic ReS₂/WSe₂ heterostructure. *Nanoscale* **14**, 10851-10861 (2022).
13. Dirnberger, F., Ziegler, J. D., Faria Junior, P. E., Bushati, R., Taniguchi, T., Watanabe, K., Fabian, J., Bougeard, D., Chernikov, A. & Menon, V. M. Quasi-1D exciton channels in strain-engineered 2D materials. *Sci. Adv.* **7**, eabj3066 (2021).
14. Coriolano, A., Polimeno, L., Pugliese, M., Cannavale, A., Trypogeorgos, D., Di Renzo, A., Ardizzone, V., Rizzo, A., Ballarini, D., Gigli, G., Maiorano, V., Rosyadi, A. S.,

- Chuang, C.-A., Ho, C.-H., Marco, L. D., Sanvitto, D. & Giorgi, M. D. Rydberg polaritons in ReS₂ crystals. *Sci. Adv.* **8** (47), eadd8857 (2022).
15. Sim, S., Lee, D., Trifonov, A.V., Kim, T., Cha, S., Sung, J.H., Cho, S., Shim, W., Jo, M.H. & Choi, H. Ultrafast quantum beats of anisotropic excitons in atomically thin ReS₂. *Nat. Commun.* **9**, 351 (2018).
 16. Island, J. O., Steele, G. A., van der Zant, H. S. & Castellanos-Gomez, A. Environmental instability of few-layer black phosphorus. *2D Mater.* **2**, 011002 (2015).
 17. Kuriakose, S., Ahmed, T., Balendhran, S., Bansal, V., Sriram, S., Bhaskaran, M. & Walia, S. Black phosphorus: ambient degradation and strategies for protection. *2D Mater.* **5**, 032001 (2018).
 18. Liu, E., Fu, Y., Wang, Y., Feng, Y., Liu, H., Wan, X., Zhou, W., Wang, B., Shao, L., Ho, C. H., Huang, Y. S., Cao, Z., Wang, L., Li, A., Zeng, J., Song, F., Wang, X., Shi, Y., Yuan, H., Hwang, H. Y., Cui, Y., Miao F. & Xing D. Integrated digital inverters based on two-dimensional anisotropic ReS₂ field-effect transistors. *Nat. Commun.* **6**, 6991 (2015).
 19. Wang, J., Zhou, Y. J., Xiang, D., Ng, S. J., Watanabe, K., Taniguchi, T. & Eda, G. Polarized Light-Emitting Diodes Based on Anisotropic Excitons in Few-Layer ReS₂. *Adv. Mater.* **32**, 2001890 (2020).
 20. Kapuściński, P., Dzian, J., Slobodeniuk, A. O., Rodríguez-Fernández, C., Jadczyk, J., Bryja, L., Faugeras, C., Basko, D. M. & Potemski, M. Exchange-split multiple Rydberg series of excitons in anisotropic quasi two-dimensional ReS₂. *2D Mater.* **9**, 045005 (2022).
 21. Oliva, R., Laurien, M., Dybala, F., Kopaczek, J., Qin, Y., Tongay, S., Rubel, O. & Kudrawiec, R. Pressure dependence of direct optical transitions in ReS₂ and ReSe₂. *NPJ 2D Mater. Appl.* **3**, 20 (2019).
 22. Sim, S., Lee, D., Lee, J., Bae, H., Noh, M., Cha, S., Jo, M.H., Lee, K. & Choi, H. Light polarization-controlled conversion of ultrafast coherent–incoherent exciton dynamics in few-layer ReS₂. *Nano Lett.* **19**, 7464–7469 (2019).
 23. Cui, Q., He, J., Bellus, M.Z., Mirzokarimov, M., Hofmann, T., Chiu, H.Y., Antonik, M., He, D., Wang, Y. & Zhao, H. Transient absorption measurements on anisotropic monolayer ReS₂. *Small* **11**, 5565–5571 (2015).
 24. Wang, X., Shinokita, K., Lim, H. E., Mohamed, N. B., Miyauchi, Y., Cuong, N. T., Okada, S. & Matsuda, K. Direct and indirect exciton dynamics in few-layered ReS₂ revealed by photoluminescence and pump-probe spectroscopy. *Adv. Funct. Mater.* **29**, 1806169 (2019).
 25. He, J., Zhang, L., He, D., Wang, Y., He, Z. & Zhao, H. Ultrafast Transient Absorption Measurements of Photocurrent Dynamics in Monolayer and Bulk ReSe₂. *Opt. Express* **26**, 21501 (2018).
 26. Ge, Y., Tan, J., Xu, G., Feng, X., Li, E., Wang, Y., Lu, C. & Xu, X. Ultrafast Charge Transfer-Induced Unusual Nonlinear Optical Response in ReSe₂/ReS₂ Heterostructure. *ACS Nano* (2024), DOI: 10.1021/acsnano.4c11372.

27. Dey, P., Paul, J., Wang, Z., Stevens, C. E., Liu, C., Romero, A. H., Shan, J., Hilton, D. J. & Karaiskaj, D. Optical coherence in atomic-monolayer transition-metal dichalcogenides limited by electron-phonon interactions. *Phys. Rev. Lett.* **116**, 127402 (2016).
28. Moody, G., Kavir Dass, C., Hao, K., Chen, C. H., Li, L. J., Singh, A., Tran, K., Clark, G., Xu, X., Berghäuser, G., Malic, E., Knorr, A. & Li, X. Intrinsic homogeneous linewidth and broadening mechanisms of excitons in monolayer transition metal dichalcogenides. *Nat. Commun.* **6**, 8315 (2015).
29. Jakubczyk, T., Delmonte, V., Koperski, M., Nogajewski, K., Faugeras, C., Langbein, W., Potemski, M. & Kasprzak, J. Radiatively limited dephasing and exciton dynamics in MoSe₂ monolayers revealed with four-wave mixing microscopy. *Nano Lett.* **16**, 5333-5339 (2016).
30. Jakubczyk, T., Nogajewski, K., Molas, M. R., Bartos, M., Langbein, W., Potemski, M. & Kasprzak, J. Impact of environment on dynamics of exciton complexes in a WS₂ monolayer. *2D Mater.* **5**, 031007 (2018).
31. Jakubczyk, T., Nayak, G., Scarpelli, L., Liu, W. L., Dubey, S., Bendiab, N., Marty, L., Taniguchi, T., Watanabe, K., Masia, F., Nogues, G., Coraux, J., Langbein, W., Renard, J., Bouchiat, V. & Kasprzak, J. Coherence and density dynamics of excitons in a single-layer MoS₂ reaching the homogeneous limit. *ACS Nano* **13**, 3500-3511 (2019).
32. Boule, C., Vaclavkova, D., Bartos, M., Nogajewski, K., Zdražil, L., Taniguchi, T., Watanabe, K., Potemski, M. & Kasprzak, J. Coherent dynamics and mapping of excitons in single-layer MoSe₂ and WSe₂ at the homogeneous limit. *Phys. Rev. Mater.* **4**, 034001 (2020).
33. Smallwood, C. L. & Cundiff, S. T. Multidimensional coherent spectroscopy of semiconductors. *Laser Photonics Rev.* **12**, 1800171 (2018).
34. Shah, J. *Ultrafast Spectroscopy of Semiconductors and Semiconductor Nanostructures.* Springer (1996).
35. Lin, Y. C., Komsa, H. P., Yeh, C. H., Bjorkman, T., Liang, Z. Y., Ho, C. H., Huang, Y. S., Chiu, P. W., Krasheninnikov, A. V. & Suenaga, K. Single-layer ReS₂: two-dimensional semiconductor with tunable in-plane anisotropy. *ACS Nano* **9**, 11249-11257 (2015).
36. Chenet, D. A., Aslan, B., Huang, P. Y., Fan, C., Van Der Zande, A. M., Heinz, T. F. & Hone, J. C. In-plane anisotropy in mono- and few-layer ReS₂ probed by Raman spectroscopy and scanning transmission electron microscopy. *Nano Lett.* **15**, 5667-5672 (2015).
37. Fras, F., Mermillod, Q., Nogues, G., Hoarau, C., Schneider, C., Kamp, M., Höfling, S., Langbein, W. & Kasprzak, J. Multi-wave coherent control of a solid-state single emitter. *Nat. Photonics* **10**, 155-158 (2016).
38. Ho, C. H. & Liu, Z. Z. Complete-series excitonic dipole emissions in few layer ReS₂ and ReSe₂ observed by polarized photoluminescence spectroscopy. *Nano Energy* **56**, 641-650 (2019).

39. (Dhara 2020) Dhara, A., Chakrabarty, D., Das, P., Pattanayak, A. K., Paul, S., Mukherjee, S. & Dhara, S. Additional excitonic features and momentum-dark states in ReS₂. *Phys. Rev. B* **102**, 161404 (2020).
40. Nguyen, D. T., Voisin, C., Roussignol, P., Roquelet, C., Lauret, J. S. & Cassabois, G. Phonon-induced dephasing in single-wall carbon nanotubes. *Phys. Rev. B* **84**, 115463 (2011).
41. Yoshikawa, K., Matsunaga, R., Matsuda, K. & Kanemitsu, Y., 2009. Mechanism of exciton dephasing in a single carbon nanotube studied by photoluminescence spectroscopy. *Appl. Phys. Lett.*, **94**(9) (2009).
42. Biswas, D., Ganose, A. M., Yano, R., Riley, J. M., Bawden, L., Clark, O. J., Feng, J., Collins-Mcintyre, L., Sajjad, M. T., Meevasana, W., Kim, T. K., Hoesch, M., Rault, J. E., Sasagawa, T., Scanlon, D. O. & King, P. D. C. Narrow-band anisotropic electronic structure of ReS₂. *Phys. Rev. B* **96**, 085205 (2017).
43. Scarpelli, L., Masia, F., Alexeev, E. M., Withers, F., Tartakovskii, A. I., Novoselov, K. S. & Langbein, W. Resonantly excited exciton dynamics in two-dimensional MoSe₂ monolayers. *Phys. Rev. B* **96**, 045407 (2017).
44. Pöllmann, C., Steinleitner, P., Leierseder, U., Nagler, P., Plechinger, G., Porer, M., Bratschitsch, R., Schüller, C., Korn, T. & Huber, R. Resonant internal quantum transitions and femtosecond radiative decay of excitons in monolayer WSe₂. *Nat. Mater.* **14**, 889-893 (2015).
45. Połczyńska, K. E., Le Denmat, S., Taniguchi, T., Watanabe, K., Potemski, M., Kossacki, P., Pacuski, W. & Kasprzak, J. Coherent Imaging and Dynamics of Excitons in MoSe₂ Monolayers Epitaxially Grown on Hexagonal Boron Nitride. *Nanoscale* **15** (15), 6941–6946 (2023).
46. Helmrich, S., Sampson, K., Huang, D., Selig, M., Hao, K., Tran, K., Achstein, A., Young, C., Knorr, A., Malic, E., Woggon, U., Owschimikow, N. & Li, X. Phonon-assisted intervalley scattering determines ultrafast exciton dynamics in MoSe₂ bilayers. *Phys. Rev. Lett.* **127**, 157403 (2021).
47. Raja, A., Selig, M., Berghäuser, G., Yu, J., Hill, H. M., Rigosi, A. F., Brus, L. E., Knorr, A., Heinz, T. F., Malic, E. & Chernikov, A. Enhancement of Exciton–Phonon Scattering from Monolayer to Bilayer WS₂. *Nano Lett.* **18** (10), 6135–6143 (2018).
48. Gehlmann, M., Aguilera, I., Bihlmayer, G., Nemšák, S., Nagler, P., Gospodaric, P., Zamborlini, G., Eschbach, M., Feyer, V., Kronast, F., Młyńczak, E., Korn, T., Plucinski, L., Schüller, C., Blügel, S. & Schneider, C. M. Direct observation of the band gap transition in atomically thin ReS₂. *Nano Lett.* **17**, 5187-5192 (2017).
49. Lepetit, L., Chériaux, G. & Joffre, M. Linear Techniques of Phase Measurement by Femtosecond Spectral Interferometry for Applications in Spectroscopy. *J. Opt. Soc. Am. B* **12** (12), 2467 (1995).
50. Cundiff, S. T. Coherent spectroscopy of semiconductors. *Opt. Express* **16** (7), 4639-4664 (2008).